HAL
open science

Evidence for magnetic activity at starbirth: a powerful X-ray flare from the Class 0 protostar HOPS 383

Nicolas Grosso, Kenji Hamaguchi, David A. Principe, Joel Kastner

To cite this version:

Nicolas Grosso, Kenji Hamaguchi, David A. Principe, Joel Kastner. Evidence for magnetic activity at starbirth: a powerful X-ray flare from the Class 0 protostar HOPS 383. Astronomy and Astrophysics - A&A, 2020, 638, pp.L4. 10.1051/0004-6361/202038185 . hal-02873698

HAL Id: hal-02873698

https://hal.science/hal-02873698v1

Submitted on 18 Jun 2020

HAL is a multi-disciplinary open access archive for the deposit and dissemination of scientific research documents, whether they are published or not. The documents may come from teaching and research institutions in France or abroad, or from public or private research centers.

L'archive ouverte pluridisciplinaire **HAL**, est destinée au dépôt et à la diffusion de documents scientifiques de niveau recherche, publiés ou non, émanant des établissements d'enseignement et de recherche français ou étrangers, des laboratoires publics ou privés.

A&A 638, L4 (2020)
https://doi.org/10.1051/0004-6361/202038185
© N. Grosso et al. 2020

Astronomy & Astrophysics

LETTER TO THE EDITOR

Evidence for magnetic activity at starbirth: a powerful X-ray flare from the Class 0 protostar HOPS 383

Nicolas Grosso[1], Kenji Hamaguchi[2,3], David A. Principe[4], and Joel H. Kastner[5]

[1] Aix-Marseille Univ, CNRS, CNES, LAM, Marseille, France
e-mail: nicolas.grosso@lam.fr
[2] CRESST II and X-ray Astrophysics Laboratory NASA/GSFC, Greenbelt, MD, USA
[3] Department of Physics, University of Maryland, Baltimore County, Baltimore, MD, USA
[4] Massachusetts Institute of Technology, Kavli Institute for Astrophysics and Space Research, Cambridge, MA, USA
[5] Center for Imaging Science, School of Physics & Astronomy, and Laboratory for Multiwavelength Astrophysics, Rochester Institute of Technology, Rochester, NY, USA

Received 16 April 2020 / Accepted 2 May 2020

ABSTRACT

Context. Class 0 protostars represent the earliest evolutionary stage of solar-type stars, during which the majority of the system mass resides in an infalling envelope of gas and dust and is not yet in the central, nascent star. Although X-rays are a key signature of magnetic activity in more evolved protostars and young stars, whether such magnetic activity is present at the Class 0 stage is still debated.

Aims. We aim to detect a bona fide Class 0 protostar in X-rays.

Methods. We observed HOPS 383 in 2017 December in X-rays with the *Chandra* X-ray Observatory (~84 ks) and in near-infrared imaging with the Southern Astrophysical Research telescope.

Results. HOPS 383 was detected in X-rays during a powerful flare. This hard ($E > 2$ keV) X-ray counterpart was spatially coincident with the northwest 4 cm component of HOPS 383, which would be the base of the radio thermal jet launched by HOPS 383. The flare duration was ~3.3 h; at the peak, the X-ray luminosity reached $\sim 4 \times 10^{31}$ erg s^{-1} in the 2–8 keV energy band, a level at least an order of magnitude larger than that of the undetected quiescent emission from HOPS 383. The X-ray flare spectrum is highly absorbed ($N_{\rm H} \sim 7 \times 10^{23}$ cm^{-2}), and it displays a 6.4 keV emission line with an equivalent width of ~1.1 keV, arising from neutral or low-ionization iron.

Conclusions. The detection of a powerful X-ray flare from HOPS 383 constitutes direct proof that magnetic activity can be present at the earliest formative stages of solar-type stars.

Key words. stars: flare – stars: individual: HOPS 383 – stars: low-mass – stars: magnetic field – stars: protostars – X-rays: stars

1. Introduction

Low-mass objects that have evolved beyond the Class 0 stage are conspicuous X-ray emitters (Dunham et al. 2014), that is, Class I protostars with remnant envelopes and massive accretion disks, and Class II and III pre-main sequence stars with and without circumstellar disks (T Tauri stars). Their high luminosities ($\sim 10^{28-31}$ erg s^{-1}) compared to the solar maximum ($\sim 10^{27}$ erg s^{-1}) and their intense flaring activity in X-rays make them appear as extremely magnetically active young suns (Feigelson & Montmerle 1999; Güdel & Nazé 2009). In Class 0 protostars (André et al. 1993, 2000), the hydrostatic core is deeply embedded within its envelope and the molecular cloud, making its detection difficult at most wavelengths (Giardino et al. 2007). The most deeply-embedded X-ray sources reported in star-forming regions (Hamaguchi et al. 2005; Getman et al. 2007 and references therein; Kamezaki et al. 2014) have evolved beyond the Class 0 stage or their bolometric luminosity is not accurate enough for a robust conclusion (Appendix A). Moreover, any non-thermal radio emission from putative magnetic activity at Class 0 protostars is very likely absorbed by the bases of their ionized outflows (Güdel 2002; Dzib et al. 2013).

The object of this study in the Orion Molecular Cloud 3 (OMC-3) was identified as a protostar by a *Spitzer* survey (Megeath et al. 2012) and included in the *Herschel* Orion protostar survey (HOPS; Furlan et al. 2016) as source 383. The submillimeter to bolometric luminosity ratio of HOPS 383, 1.4% (Safron et al. 2015) well surpasses the (0.5%) threshold for bona fide Class 0 designation (André et al. 1993, 2000). Notably, HOPS 383 is the first Class 0 protostar known to have undergone a mass-accretion-driven eruption (Safron et al. 2015), which peaked by 2008 and ended by 2017 September (Appendix B).

2. Observations

We observed HOPS 383 three times with the *Chandra* X-ray Observatory (Weisskopf et al. 2002) from 2017 December 13 to 14 with simultaneous near-infrared imaging on 2017 December 14 using the 4.1 m Southern Astrophysical Research (SOAR) telescope (Krabbendam et al. 2004) in Chile.

We used *Chandra*'s Advanced CCD Imaging Spectrometer (ACIS-I) in the very faint mode with a frame time of

Open Access article, published by EDP Sciences, under the terms of the Creative Commons Attribution License (https://creativecommons.org/licenses/by/4.0), which permits unrestricted use, distribution, and reproduction in any medium, provided the original work is properly cited.

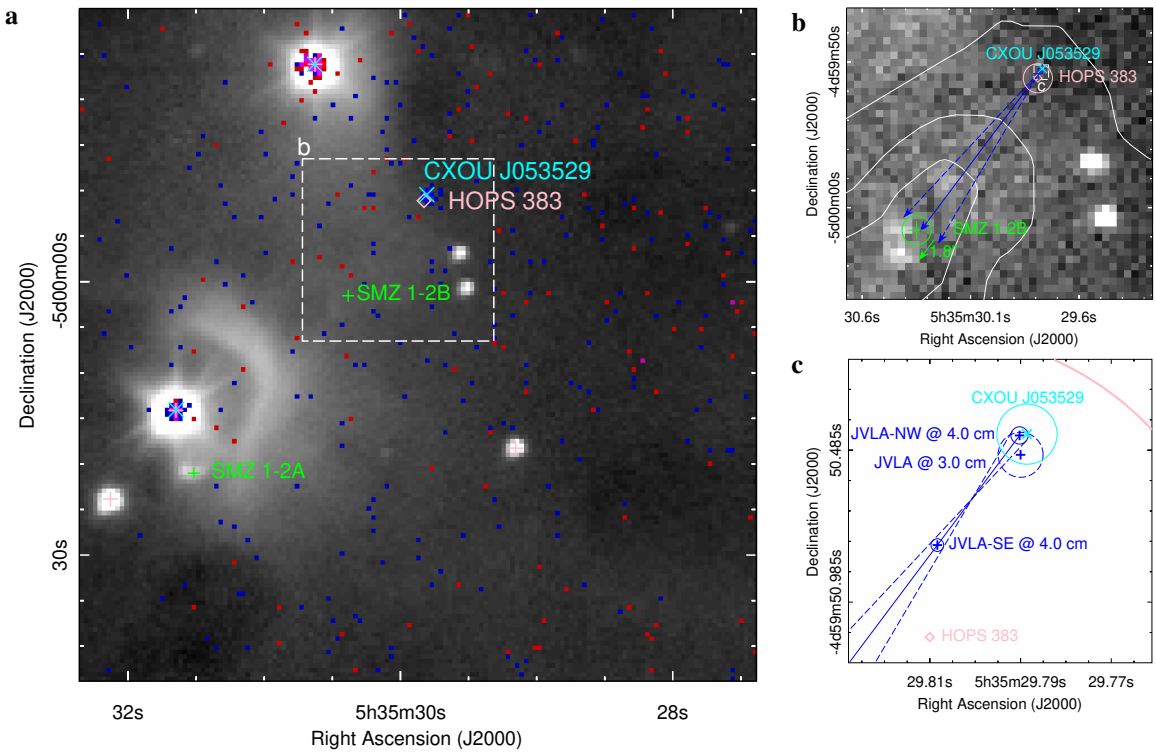

Fig. 1. *Chandra* detection of HOPS 383. *Panel a*: the red and blue 0.″492 × 0.″492 pixels display logarithmically the 0.5–2 keV and 2–7 keV X-rays, respectively, which were detected from 2017 December 13 to 14 during three ACIS-I exposures, totaling 83 877 s. The logarithmic grayscale *K*-band image was obtained on 2017 December 14 with the Spartan infrared camera on the SOAR telescope. North is up and east is left. The pink pluses and diamond, the green pluses, and cyan crosses are near- and mid-infrared sources (Megeath et al. 2012), H_2-shocked emission (Stanke et al. 2002), and X-ray sources, respectively. The white dashed box shows the field-of-view of Fig. 1b. *Panel b*: Spartan H_2-filter image obtained on 2017 December 14 in linear grayscale. The white contours show the ^{12}CO blueshifted outflow of HOPS 383 (Feddersen et al. 2020). The blue pluses are radio sources (Galván-Madrid et al. 2015; Rodríguez et al. 2017). The blue and green arrows show the direction of the thermal-jet candidate and the proper motion of the H_2 emission knot SMZ 1-2B, respectively. The white dashed box shows the field-of-view of Fig. 1c. *Panel c*: enlargement around HOPS 383 shows the mid-infrared (pink), radio (blue), and X-ray (cyan) positional error circles.

3.141 s (Appendix C.1). *Chandra* ACIS-I has on-axis a full-width half-maximum (FWHM) angular resolution of 0.″5 and a FWHM spectral resolution of 261 eV at 6.4 keV. Data reduction is described in Appendix C.2.

The SOAR Spartan infrared camera (Loh et al. 2012) is composed of 4 CCDs of 2048 × 2048 pixels. We selected the wide-field mode with a single-detector field-of-view of 2.′25 × 2.′25 (i.e., 5.′04 × 5.′04 edge-to-edge) and a pixel scale of 0.″0661 with the *K*-band and H_2 narrow-band filters. We used a five-point dithering pattern where, in the first exposure, HOPS 383 was put near the center of the northeastern detector (det3), which was then moved by 30″ from its initial position sequentially toward the south, north, west, and east in the four other exposures. This sequence was repeated until the requested exposure was achieved (Appendix D.1). Data reduction is described in Appendix D.2.

3. Near-infrared results

The near-infrared nebulosity that was prominent during the outburst (Safron et al. 2015) is not detected in our SOAR *K*-band image (Fig. 1a), indeed, it vanished by 2015 December 30 (Fischer & Hillenbrand 2017). The H_2-narrow filter image shows an emission knot of shocked molecular hydrogen at ∼15″ southeast from the mid-infrared location of HOPS 383. We identify this H_2 source with the H_2 emission knot SMZ 1-2B (Stanke et al. 2002) that was observed on 1997 September 13, yielding a proper motion of ∼1.″8 ± 1″ southeast in 20.25 yr (Fig. 1b). The corresponding velocity is $\sim(95 \pm 53) \times (\sin i/\sin 69.5°)^{-1} \times (d/420\,\mathrm{pc})\,\mathrm{km\,s^{-1}}$, where d is the distance to HOPS 383 and i is the inclination angle (90° corresponds to an edge-on view; Table 1 of Furlan et al. 2016). This is typical of the velocity values observed in the outflows from Class 0 protostars (Bontemps et al. 1996; Reipurth & Bally 2001). Assuming a constant velocity, the angular distance of ∼16″ between HOPS 383 and this emission knot corresponds to a kinematical timescale of ∼180 ± 100 yr. The proper motion direction is consistent with the orientation of the outburst nebula, the ^{12}CO blueshifted outflow (Feddersen et al. 2020), and the position angle of the binary radio counterpart of HOPS 383 at 4 cm (Galván-Madrid et al. 2015). We note that the unresolved 3 cm counterpart (Rodríguez et al. 2017) corresponds to the faint northwest component at 4 cm, JVLA-NW, which suggests that JVLA-NW would be the base of the radio thermal jet launched by HOPS 383, whereas the brighter southeast component at 4 cm, JVLA-SE, would be an emission knot along this thermal jet (Fig. 1c).

4. X-ray results

4.1. X-ray flare of HOPS 383

We detect a hard ($E > 2$ keV) X-ray source, CXOU J053529.78-045950.4 (hereafter, CXOU J053529), that is spatially

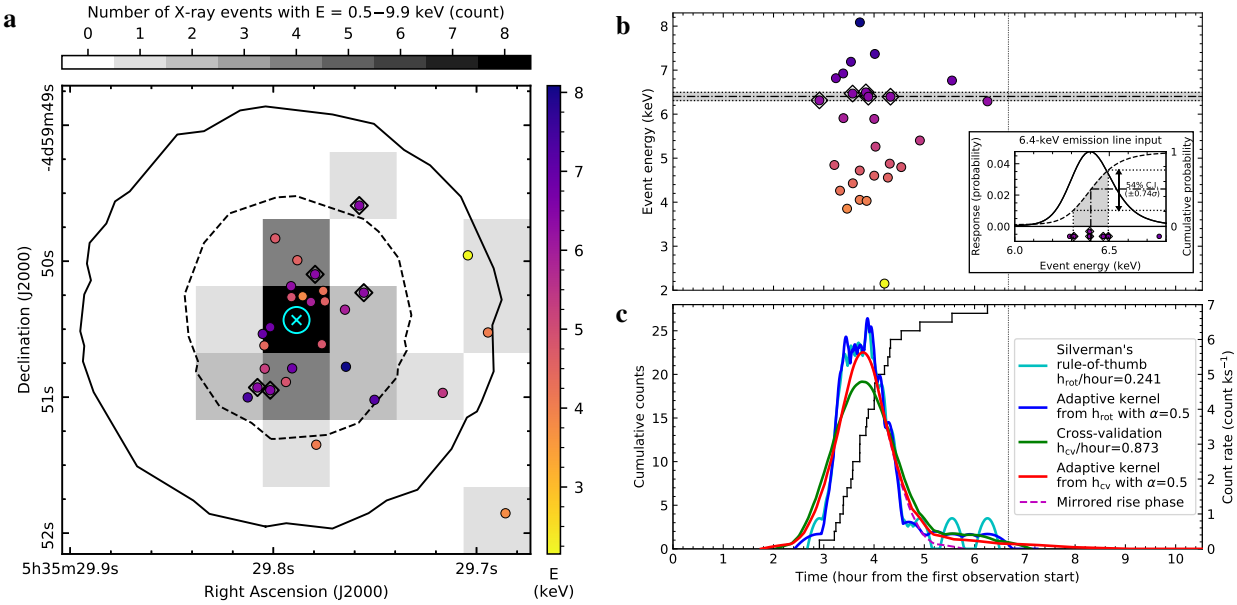

Fig. 2. X-ray flare of HOPS 383. *Panel a*: sky position of the X-ray events detected during the *Chandra* observation on 2017 December 13. The cyan cross and circle are the X-ray position and positional error of HOPS 383, respectively. The dashed and solid contours encompass 90% (position determination) and 96% (spectrum extraction) of 1.49 keV point source emission, respectively. The diamonds mark the events from the 6.4 keV emission line. *Panel b*: event energy versus time of arrival. The gray stripe is centered at 6.4 keV and corresponds to a confidence interval of 54% centered at this emission line observed with ACIS-I (inset). *Panel c*: cumulative counts and various smoothed light curves. The dashed curve is the mirrored rise phase of the red curve. *Panels b and c*: the vertical dotted line at ~6.7 h marks an exposure gap of 3.1 s.

coincident with JVLA-NW (Fig. 1 and Appendix C.3). CXOU J053529 was not detected in a *Chandra* observation of the OMC-2 and 3 region obtained in 2000 January at an off-axis angle of 6′.3 (Tsujimoto et al. 2002; Getman et al. 2017).

This spatially unresolved X-ray source is only detected, with 28 counts in the 0.5–9.9 keV energy range, during the first *Chandra* exposure that we obtained in 2017 (Fig. 2a). The first photon is detected ~2.9 h after the start of the observation and the X-ray burst duration is ~3.3 h (Fig. 2b). We estimated the shape of the light curve by smoothing the event times of arrival (Appendix C.4). The count rate peaks to ~5.6 counts ks^{-1} in ~0.9 h after the first photon detection, and it decays gradually in ~2.5 h until the last photon detection (red curve in Fig. 2c). This time variation, with rapid rise and slow decay, is similar to the typical light curves of magnetic flares from young stellar objects (YSOs; Getman et al. 2008). X-rays may also be emitted by accretion shocks at the protostellar surface and/or shocks in outflows (Güdel & Nazé 2009), but the former produces plasmas that are not bright and hot enough to emit the observed hard X-rays and the latter is constant on week timescales (Kastner et al. 2005), which is much longer than the hour variability that we observed. Therefore, this burst of X-rays indicates magnetic activity from HOPS 383 that is associated with JVLA-NW.

4.2. X-ray flare spectrum

We modeled the X-ray spectrum with isothermal coronal plasma emission suffering from intervening absorption (Appendix C.5). The best-fit model has an excess and a deficit relative to the observed spectrum below and above 6.4 keV, respectively, suggesting an additional component at 6.4 keV. This deviation is likely associated with the emission line arising from neutral or low-ionization iron. Therefore, we included in the model a Gaussian emission line centered at 6.4 keV. We performed a Markov chain Monte Carlo analysis (MCMC) to compute the probability density functions of the physical parameters, from which we determined the median parameter values and 90% confidence intervals. We find that CXOU J053529 is highly embedded with a hydrogen column density ($N_{\rm H,X}$) of $7.0^{+3.5}_{-3.1} \times 10^{23}$ cm^{-2}. This result for $N_{\rm H}$ is consistent with the large median energy of the 0.5–8 keV counts (MedE = 5.402 keV)[1], given the log $N_{\rm H}$ versus MedE relations found for YSOs in the Orion nebula cluster (ONC; Fig. 8 of Feigelson et al. 2005) and M17 (Fig. 10a of Getman et al. 2010).

We detected the 6.4 keV emission line with a high probability of 98.9%. Our spectral analysis suggests that we have detected five photons from the Fe 6.4 keV emission line; these photons are likely the closest in energy to 6.4 keV. Indeed, we observed five photons with energies that are densely packed around the predicted emission feature at 6.4 keV (diamonds in Fig. 2b inset). Moreover, the spatial distribution of these Fe line photons is point-like (Fig. 2a), suggesting all of the observed Fe fluorescence emission arises from within the *Chandra* point spread function (PSF), that is to say, a radius from HOPS 383 that is lower than 105 au at the assumed distance to the protostar. The iron line equivalent width, EW = $1.1^{+2.1}_{-0.9}$ keV, is large (even at the lower limit) relative to what was expected from the possible emission processes. The neutral iron can be ionized by photons or electrons that have energies larger than the Fe K-shell ionization potential of 7.112 keV. The contributions of these two ionization channels to the observed X-ray line in accreting young stars and Class I protostars (Güdel & Nazé 2009; Hamaguchi et al. 2005, 2010; Czesla & Schmitt 2010; Pillitteri et al. 2019) are not firmly settled, but photoionization

[1] For epoch 2017, the degradation of the ACIS effective area at low energy due to the contamination of the optical blocking filter likely does not significantly modify the median energy of a source as hard as HOPS 383.

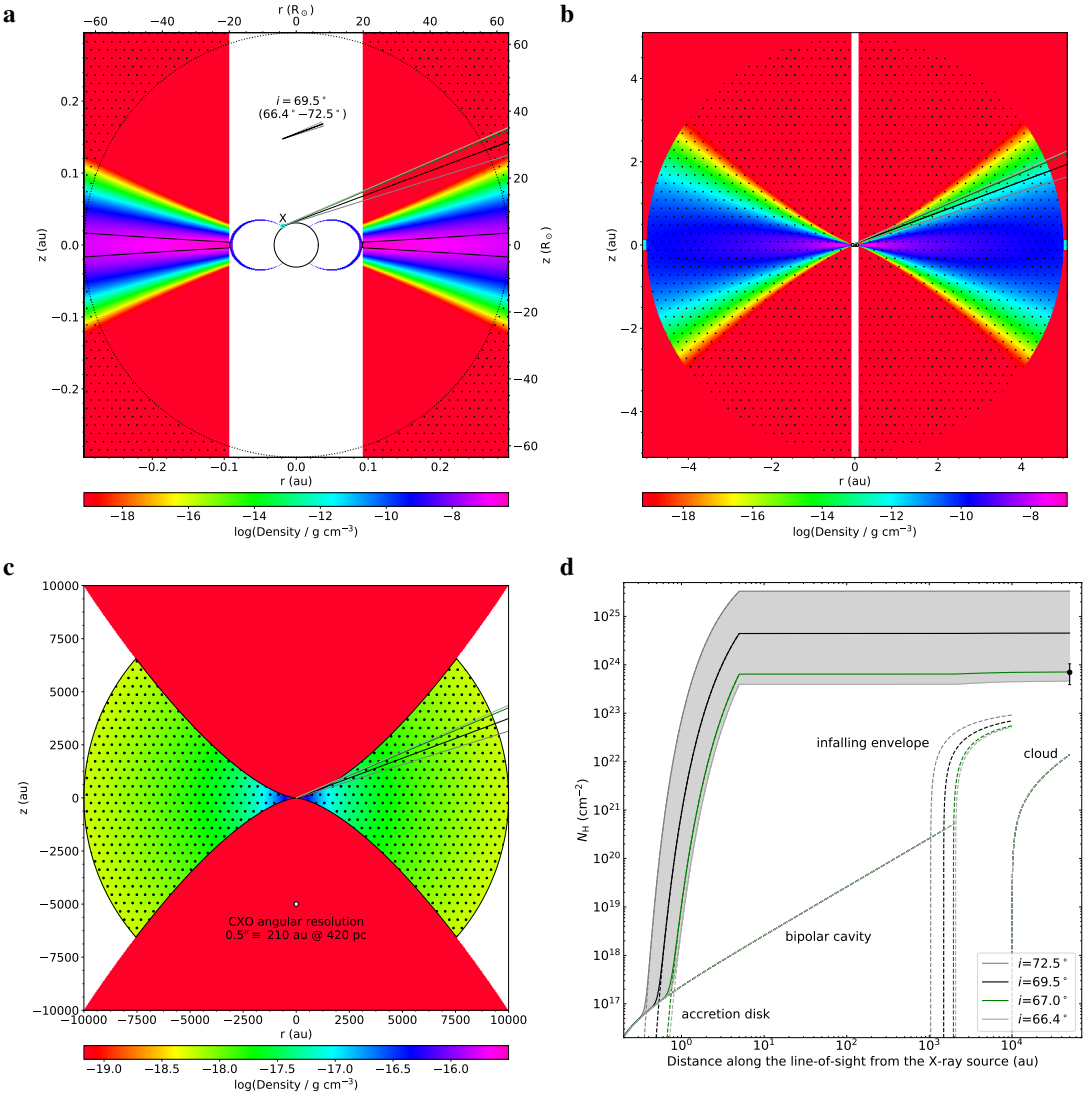

Fig. 3. Probing the gas and dust toward HOPS 383 with the X-ray spectrum. *Panels a–c*: 2D density distribution from small to large spatial scales and viewing angle from the model of HOPS 383 (Furlan et al. 2016). Dots indicate regions with dust. *Panel d*: cumulative hydrogen column density along the line-of-sight from the X-ray source. The dashed lines show the contribution of the accretion disk, the bipolar cavity, the infalling envelope, and the cloud. The data point with an error bar (90% C.I.) is the hydrogen column density that we obtained from the X-ray spectrum modeling.

is less energetically challenging (Czesla & Schmitt 2010). The plasma temperature is not well constrained mainly due to the low count rate, but a hot plasma temperature is favored ($kT = 4.1^{+13.8}_{-2.8}$ keV), which is consistent with a magnetic flare and the photoionization of iron.

4.3. X-ray flare energetics

The mean value of the absorption-corrected luminosity during the flare time interval is $1.7^{+5.5}_{-1.1} \times 10^{31}$ erg s^{-1} in the 2–8 keV energy band. Multiplying this value by the flare peak to flare mean count rate ratio (2.39) provides the flare peak value of $\sim 4.2^{+13.0}_{-2.6} \times 10^{31}$ erg s^{-1}. For comparison purposes, the maximum peak value of the 84 X-ray flares with typical shapes observed from YSOs in the ONC (Getman et al. 2008) is 8.3×10^{32} erg s^{-1} in the 0.5–8 keV energy band; only ~34% of these flares have peak values that are higher than the HOPS 383 one. During our observations, the non-detection of HOPS 383 outside the flare time interval implies that its quiescent absorption-corrected luminosity is lower than 2.0×10^{30} erg s^{-1} in the 2–8 keV energy band (Appendix C.6). Therefore, the flare that we detected peaked at least 21^{+65}_{-13} times above the quiescent level. The lower limit on the total energy released in X-rays during this flare, as computed from the mean luminosity times the flare duration, was $2.0^{+6.6}_{-1.3} \times 10^{35}$ erg s^{-1}.

5. Discussion

Starting from a model of HOPS 383 consisting of an infalling envelope with bipolar cavities carved by outflows and a small (5 au radius) accretion disk (Figs. 3a–c), constrained by the post-outburst spectral energy distribution (SED) using a Monte Carlo radiative transfer code (Furlan et al. 2016), we computed the predicted $N_{\rm H}$ toward the central protostar (Appendix E). Due to the high inclination angle in this model, the line-of-sight intercepts the upper layers of the accretion disk, which produce the bulk of $N_{\rm H}$; moreover, this value is extremely sensitive to the viewing angle (Fig. 3d). The observed $N_{\rm H,X}$ favors a slightly lower

inclination. However, the available grid of protostellar models (Furlan et al. 2016) does not include a lower-mass accretion disk or a model with no accretion disk at all, which may reproduce both the SED and $N_{\rm H,X}$. These model trials illustrate the importance of X-ray constraints on $N_{\rm H}$ to the overall consistency of protostar modeling.

In the optically thin case at 6.4 keV, that is to say, as long as the H column density by a cold absorber with a solar elemental abundance ($N'_{\rm H}$) is lower than $\sim 10^{24}\,{\rm cm}^{-2}$, the iron line EW produced by photoionization is ${\rm EW} = 2.5\,(\Omega/4\pi)\,(N'_{\rm H}/10^{22}\,{\rm cm}^{-2})$ eV, where Ω is the subtended angle of the irradiated material from the X-ray irradiating source (Tsujimoto et al. 2005). Since $\Omega/4\pi < 1$, the large observed value of EW in HOPS 383 rules out the optically thin condition. In the optically thick case of the photoionization of photospheric iron by an X-ray flare, the iron line EW that is computed by Monte-Carlo radiative transfer simulations is limited to ~130 eV for solar iron abundance and can only be increased by factors <2 by disk flaring (Drake et al. 2008). However, large iron line EW can be obtained in both optical depth conditions when the photoionizing X-ray source is partly eclipsed (Drake et al. 2008). In the model, the X-ray source is located on the obscured region of the star and near the base of the accretion funnels (Fig. 3a). This source irradiates the accretion funnels, the upper layers of the accretion disk (Fig. 3b), and the circumstellar envelope (Fig. 3c).

6. Conclusions

Our detection of an X-ray flare from HOPS 383 provides conclusive evidence that strong magnetic activity is present at this bona fide Class 0 protostar. The resulting X-ray irradiation contributes to the ionization of the base of the outflow (Shang et al. 2004), and the magnetic reconnection that triggers powerful flares, similar to the one we detected, most likely drives energetic particle ejections (Feigelson et al. 2002). Such protostellar cosmic rays have been proposed to collide with refractory dust grains located at the inner edge of the accretion disk, inducing spallation reactions that could yield short-lived radionuclei, such as are observed in the refractory inclusions of chondritic meteorites (Gounelle et al. 2013; Sossi et al. 2017). Mass ejections have similarly been invoked in the case of the bona fide Class 0 protostar OMC-2 FIR 4 to explain the production of free electrons via collisions in the envelope, thereby enhancing the abundances of molecular ions (Ceccarelli et al. 2014). The Class 0 stage (~10 000 yr) has an ~10 times shorter duration than the Class I stage; however, during the earliest stage, half of the envelope mass is accreted, building the central star and the accretion disk. Therefore, the determination of the internal irradiation level in Class 0 protostars is paramount for the understanding of protostellar chemistry.

Longer observations are required to determine the flaring activity level and to collect more photons from such deeply-embedded, nascent stars. *Athena* X-IFU (Barret et al. 2018), which is scheduled to be launched at the beginning of the 2030s, will improve the X-ray throughput and spectral resolution at 6.4 keV, enabling a potential leap in our knowledge of the onset of protostellar magnetic activity.

Acknowledgements. We thank the anonymous referee for the careful reading of the manuscript. We are grateful to Joshua Wing (*Chandra* X-ray Center; CXC) and Steve Heathcote (Director of the Cerro Tololo Inter-American Observatory) for the scheduling of the simultaneous *Chandra* and SOAR observations. K.H., D.P., and N.G. are thankful to Jonathan (Jay) Elias (SOAR Director) and Patricio Ugarte (Observer Support) for technical support during the Spartan observation. N.G. thanks Patrick Broos and Leisa Townsley for Acis Extract support. This work was supported by "the Programme National de Physique Stellaire" (PNPS) of CNRS/INSU co-funded by CEA and CNES. Support for this work was provided by the National Aeronautics and Space Administration (NASA) through *Chandra* Award Numbers GO7-18012A and B issued by the CXC, which is operated by the Smithsonian Astrophysical Observatory for and on behalf of the NASA under contract NAS8-03060. The scientific results reported in this article are based on observations made by the *Chandra* X-ray Observatory (ObsIDs 18927, 20882 and 20883). This research has made use of software provided by the CXC in the application packages CIAO. SOAR is a joint project of the Ministério da Ciência, Tecnologia, e Inovação (MCTI) da República Federativa do Brasil, the US National Optical Astronomy Observatory (NOAO), the University of North Carolina at Chapel Hill (UNC), and Michigan State University (MSU). This publication makes use of data products from WISE, which is a joint project of the University of California (Los Angeles) and the Jet Propulsion Laboratory/California Institute of Technology (JPL/Caltech), and NEOWISE which is a project of the JPL/Caltech. WISE and NEOWISE are funded by the NASA. This work has made use of data from the European Space Agency (ESA) mission *Gaia* (https://www.cosmos.esa.int/web/gaia), processed by the *Gaia* Data Processing and Analysis Consortium (DPAC, https://www.cosmos.esa.int/web/gaia/dpac/consortium). Funding for the DPAC has been provided by national institutions, in particular the institutions participating in the *Gaia* Multilateral Agreement. This research has made use of Python and astropy, corner, matplotlib, numpy, pyregion, scipy and statsmodels modules.

References

André, P., & Montmerle, T. 1994, ApJ, 420, 837
André, P., Ward-Thompson, D., & Barsony, M. 1993, ApJ, 406, 122
André, P., Ward-Thompson, D., & Barsony, M. 2000, in Protostars & Planets IV, eds. V. Mannings, A. P. Boss, & S. S. Russell (Tucson: University of Arizona Press), 59
André, P., Minier, V., Gallais, P., et al. 2008, A&A, 490, L27
Barret, D., Lam Trong, T., den Herder, J.-W., et al. 2018, in Space Telescopes and Instrumentation 2018: Ultraviolet to Gamma Ray, SPIE Conf. Ser., 10699, 106991G
Bertin, E., & Arnouts, S. 1996, A&AS, 117, 393
Bertin, E., Mellier, Y., Radovich, M., et al. 2002, in Astronomical Data Analysis Software and Systems XI, eds. D. A. Bohlender, D. Durand, & T. H. Handley, ASP Conf. Ser., 281, 228
Bontemps, S., André, P., Terebey, S., & Cabrit, S. 1996, A&A, 311, 858
Broos, P. S., Townsley, L. K., Feigelson, E. D., et al. 2010, ApJ, 714, 1582
Ceccarelli, C., Dominik, C., López-Sepulcre, A., et al. 2014, ApJ, 790, L1
Czesla, S., & Schmitt, J. H. M. M. 2010, A&A, 520, A38
D'Alessio, P., Canto, J., Calvet, N., & Lizano, S. 1998, ApJ, 500, 411
Davis, J. E., Bautz, M. W., Dewey, D., et al. 2012, in Space Telescopes and Instrumentation 2012: Ultraviolet to Gamma Ray, SPIE Conf. Ser., 8443, 84431A
Drake, J. J., Ercolano, B., & Swartz, D. A. 2008, ApJ, 678, 385
Dunham, M. M., Stutz, A. M., Allen, L. E., et al. 2014, in Protostars & Planets VI, eds. H. Beuther, R. Klessen, C. Dullemond, & T. Henning (Tucson: Univ. of Arizona Press), 195
Dzib, S. A., Loinard, L., Mioduszewski, A. J., et al. 2013, ApJ, 775, 63
Feddersen, J. R., Arce, H. G., Kong, S., et al. 2020, ApJ, submitted [arXiv:2004.03504]
Feigelson, E. D., & Jogesh Babu, G. 2012, Modern Statistical Methods for Astronomy (Cambridge: Cambridge University Press)
Feigelson, E. D., & Montmerle, T. 1999, ARA&A, 37, 363
Feigelson, E. D., Garmire, G. P., & Pravdo, S. H. 2002, ApJ, 572, 335
Feigelson, E. D., Getman, K., Townsley, L., et al. 2005, ApJS, 160, 379
Fischer, W. J., & Hillenbrand, L. 2017, ATel, 9969, 1
Foreman-Mackey, D., Hogg, D. W., Lang, D., & Goodman, J. 2013, PASP, 125, 306
Fruscione, A., McDowell, J. C., Allen, G. E., et al. 2006, in Observatory Operations: Strategies, Processes, and Systems, SPIE Conf. Ser., 6270, 62701V
Furlan, E., Fischer, W. J., Ali, B., et al. 2016, ApJS, 224, 5
Gaia Collaboration (Prusti, T., et al.) 2016, A&A, 595, A1
Gaia Collaboration (Brown, A. G. A., et al.) 2018, A&A, 616, A1
Galván-Madrid, R., Rodríguez, L. F., Liu, H. B., et al. 2015, ApJ, 806, L32
Getman, K. V., Feigelson, E. D., Garmire, G., Broos, P., & Wang, J. 2007, ApJ, 654, 316
Getman, K. V., Feigelson, E. D., Broos, P. S., Micela, G., & Garmire, G. P. 2008, ApJ, 688, 418
Getman, K. V., Feigelson, E. D., Broos, P. S., Townsley, L. K., & Garmire, G. P. 2010, ApJ, 708, 1760
Getman, K. V., Broos, P. S., Kuhn, M. A., et al. 2017, ApJS, 229, 28

Giardino, G., Favata, F., Micela, G., Sciortino, S., & Winston, E. 2007, A&A, 463, 275
Goodman, J., & Weare, J. 2010, Commun. Appl. Math. Comput. Sci., 5, 65
Gounelle, M., Chaussidon, M., & Rollion-Bard, C. 2013, ApJ, 763, L33
Groppi, C. E., Hunter, T. R., Blundell, R., & Sandell, G. 2007, ApJ, 670, 489
Güdel, M. 2002, ARA&A, 40, 217
Güdel, M., & Nazé, Y. 2009, A&ARv, 17, 309
Güdel, M., Briggs, K. R., Arzner, K., et al. 2007, A&A, 468, 353
Hamaguchi, K., Corcoran, M. F., Petre, R., et al. 2005, ApJ, 623, 291
Hamaguchi, K., Grosso, N., Kastner, J. H., Weintraub, D. A., & Richmond, M. 2010, ApJ, 714, L16
Hartmann, L., Hewett, R., & Calvet, N. 1994, ApJ, 426, 669
Hogg, D. W., & Foreman-Mackey, D. 2018, ApJS, 236, 11
Kamezaki, T., Imura, K., Omodaka, T., et al. 2014, ApJS, 211, 18
Kastner, J. H., Franz, G., Grosso, N., et al. 2005, ApJS, 160, 511
Krabbendam, V. L., Heathcote, S., Schumacher, G., et al. 2004, Proc. SPIE, 5489, 615
Loh, E. D., Biel, J. D., Davis, M. W., et al. 2012, PASP, 124, 343
Mainzer, A., Bauer, J., Cutri, R. M., et al. 2014, ApJ, 792, 30
Marrese, P. M., Marinoni, S., Fabrizio, M., & Altavilla, G. 2019, A&A, 621, A144
Megeath, S. T., Gutermuth, R., Muzerolle, J., et al. 2012, AJ, 144, 192
Navarete, F., Damineli, A., Barbosa, C. L., & Blum, R. D. 2015, MNRAS, 450, 4364
Ormel, C. W., Min, M., Tielens, A. G. G. M., Dominik, C., & Paszun, D. 2011, A&A, 532, A43
Palla, F., & Stahler, S. W. 1992, ApJ, 392, 667
Palla, F., & Stahler, S. W. 1999, ApJ, 525, 772
Pillitteri, I., Sciortino, S., Reale, F., et al. 2019, A&A, 623, A67
Reipurth, B., & Bally, J. 2001, ARA&A, 39, 403
Rodríguez, L. F., Zapata, L. A., & Palau, A. 2017, AJ, 153, 209
Safron, E. J., Fischer, W. J., Megeath, S. T., et al. 2015, ApJ, 800, L5
Saraceno, P., André, P., Ceccarelli, C., Griffin, M., & Molinari, S. 1996, A&A, 309, 827
Schirmer, M. 2013, ApJS, 209, 21
Shang, H., Lizano, S., Glassgold, A., & Shu, F. 2004, ApJ, 612, L69
Smith, R. K., Brickhouse, N. S., Liedahl, D. A., & Raymond, J. C. 2001, ApJ, 556, L91
Sossi, P. A., Moynier, F., Chaussidon, M., et al. 2017, Nat. Astron., 1, 0055
Stahler, S. W. 1988, ApJ, 332, 804
Stanke, T., McCaughrean, M. J., & Zinnecker, H. 2002, A&A, 392, 239
Taylor, M. B. 2019, in Astronomical Data Analysis Software and Systems XXVII, eds. P. J. Teuben, M. W. Pound, B. A. Thomas, & E. M. Warner, ASP Conf. Ser., 523, 43
Tsujimoto, M., Koyama, K., Tsuboi, Y., Goto, M., & Kobayashi, N. 2002, ApJ, 566, 974
Tsujimoto, M., Feigelson, E. D., Grosso, N., et al. 2005, ApJS, 160, 503
Weisskopf, M. C., Brinkman, B., Canizares, C., et al. 2002, PASP, 114, 1
Whitney, B. A., Wood, K., Bjorkman, J. E., & Wolff, M. J. 2003, ApJ, 591, 1049
Wilms, J., Allen, A., & McCray, R. 2000, ApJ, 542, 914
Wright, E. L., Eisenhardt, P. R. M., Mainzer, A. K., et al. 2010, AJ, 140, 1868

Appendix A: Protostellar evolutionary stage

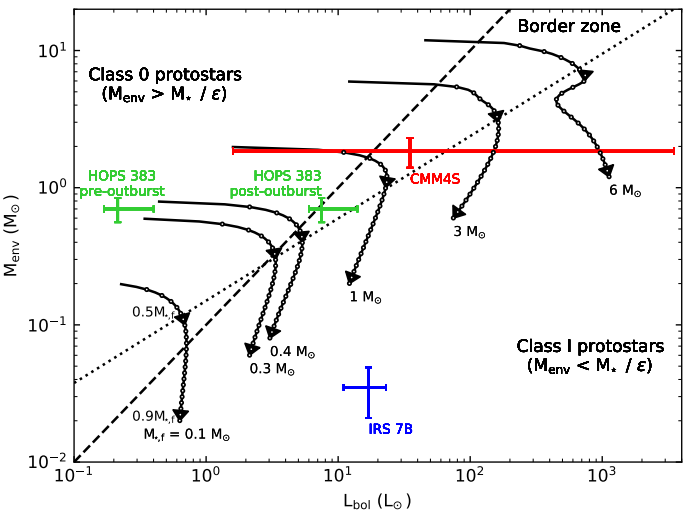

Fig. A.1. Envelope mass versus bolometric-luminosity diagram comparing the pre- and post-outburst positions of HOPS 383 (green data) with previously reported Class 0/I low-mass protostars detected in X-rays (blue and red data). The border zone between Class 0 ($M_{\rm env} > M_\star/\epsilon$, where $\epsilon = 0.5$ is the local star-formation efficiency) and Class I ($M_{\rm env} < M_\star/\epsilon$) protostars is defined by $M_{\rm env} = 0.1\,L_{\rm bol}$ (constant accretion; dotted line) and $M_{\rm env} = 0.15\,L_{\rm bol}{}^{0.6}$ (exponentially decaying accretion; dashed line). The protostellar evolutionary tracks are shown from $0.01\,M_{\star,\rm f}$ to $0.9\,M_{\star,\rm f}$, where $M_{\star,\rm f}$ is the final stellar mass. The rising time along the tracks is indicated by white dots every 10 000 yr.

Figure A.1 shows the envelope mass ($M_{\rm env}$) versus bolometric-luminosity ($L_{\rm bol}$) diagram, which is used as an evolutionary diagnostic (Saraceno et al. 1996; André et al. 2000, 2008). In this scenario, the Class 0 and I border zone is defined by $M_{\rm env} = 0.1\,L_{\rm bol}$ (constant accretion, see André & Montmerle 1994) and $M_{\rm env} = 0.15\,L_{\rm bol}{}^{0.6}$ (exponentially decaying accretion, see Bontemps et al. 1996). Propagating the model and flux uncertainties of HOPS 383 (Safron et al. 2015), we gather that: $M_{\rm env} = 0.70 \pm 0.14\,M_\odot$, $L_{\rm bol}^{\rm post\text{-}outburst} = 7.5^{+6.5}_{-1.5}\,L_\odot$, and $L_{\rm bol}^{\rm pre\text{-}outburst} = 0.21^{+0.19}_{-0.05}\,L_\odot$ (obtained from the preoutburst-to-outburst flux ratio at 24 microns of 35 ± 3). The post-outburst position of HOPS 383 is within this Class 0 and I border zone due to its high accretion luminosity, but the pre-outburst position of HOPS 383 is well above it, where $M_{\rm env}$ is larger than $M_\star$, confirming its bona fide Class 0 stage. For comparison purposes, the infrared source IRS 7B in the R Coronae Australis star-forming core, which has a deeply embedded ($N_{\rm H} \sim 3 \times 10^{23}$ cm^{-2}) X-ray counterpart that was proposed as a Class 0 protostar candidate (Hamaguchi et al. 2005), is on the side of the Class I stage in this plot, based on the bolometric luminosity reported in Groppi et al. (2007). The bolometric luminosity of the Class 0 candidate CMMS4 (Kamezaki et al. 2014) is not accurate enough for a robust conclusion.

We computed the protostellar evolutionary tracks assuming the following (Bontemps et al. 1996; André et al. 2000, 2008): an initial envelope mass, $M_{\rm env}(0)$, decays exponentially with a characteristic timescale, $\tau = 10^5$ yr; a mass accretion rate, $\dot{M}_{\rm acc}(t) = \epsilon M_{\rm env}(t)/\tau$, where the local star-formation efficiency is $\epsilon = 0.5$ (André et al. 2008); and $L_{\rm bol}(t) = L_{\rm acc}(t) + L_\star(t)$, where $L_{\rm acc}(t) = G\dot{M}_{\rm acc}(t)M_\star(t)/R_\star(t)$ is the accretion luminosity, where G is the gravitational constant, and $M_\star$(t), $R_\star(t)$, and $L_\star(t)$ are the protostellar mass, radius, and interior stellar luminosity, respectively, on the birthline of Fig. 1 in Palla & Stahler (1999) where a constant accretion rate of $10^{-5}\,M_\odot\,{\rm yr}^{-1}$ is assumed to compute the radius-mass relation (Stahler 1988; Palla & Stahler 1992). We estimate with this toy model that the final stellar mass of HOPS 383 will be ~0.4 $M_\odot$ and that less than ~10% of it has already been accreted onto the central protostar.

Appendix B: WISE and NEOWISE-R photometry

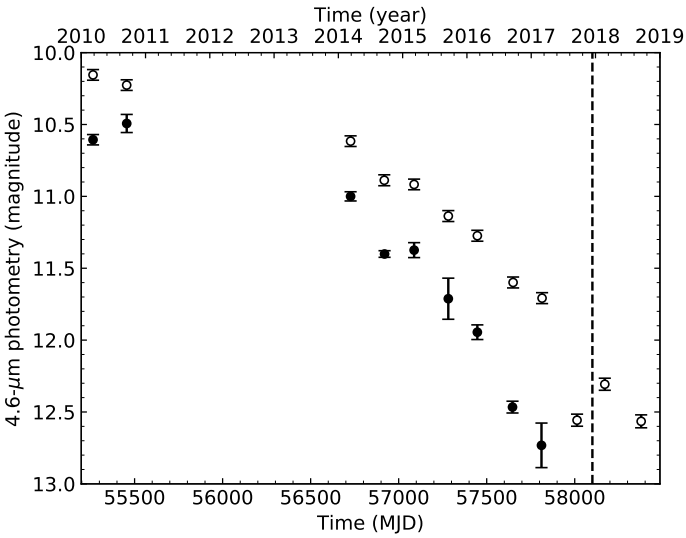

Fig. B.1. Decay of the episodic accretion of HOPS 383 in the mid-infrared. The 2010 and 2014–2018 data points are from WISE and NEOWISE observations with the W2 filter at 4.6 μm, respectively. The black and white dots are the profile-fit (Table B.1) and aperture (Table B.2) photometry for each observing epoch, respectively. The dashed vertical line is the arrival time of the first detected photon of the X-ray flare.

Table B.1. WISE and NEOWISE-R 4.6 μm profile-fit photometry of HOPS 383.

Instrument	⟨MJD⟩	ΔMJD (day)	N	⟨w2mpro⟩ (mag)	σ (mag)
WISE	55 263.89	0.99	6	10.606	0.036
WISE	55 455.31	0.73	6	10.493	0.063
NEOWISE-R	56 726.88	4.54	8	11.000	0.032
NEOWISE-R	56 919.85	0.72	7	11.401	0.023
NEOWISE-R	57 087.73	0.99	10	11.374	0.052
NEOWISE-R	57 281.88	1.12	8	11.712	0.143
NEOWISE-R	57 446.82	0.98	7	11.945	0.051
NEOWISE-R	57 646.54	0.13	2	12.466	0.041
NEOWISE-R	57 811.16	0.26	2	12.732	0.155

Notes. The profile-fit photometry was computed from the single-exposure (L1b) source tables using the mean and standard deviation of the N profile-fit fluxes in the W2 band (w2mpro) obtained during each observing epoch. We note that ΔMJD is the time interval between the first and the last frame for each epoch.

The mid-infrared flux of HOPS 383 started to rise between 2004 and 2006, peaked by 2008 with a 24 μm flux that was 35 times brighter than the pre-outburst flux, and showed no large decay between 2009 and 2012 (Safron et al. 2015). The sky position of HOPS 383 was scanned in mid-infrared twice per year by the Wide-field Infrared Survey Explorer (WISE) mission (Wright et al. 2010) in 2010 and by the Near-Earth Object

Table B.2. WISE and NEOWISE-R 4.6 μm aperture photometry of HOPS 383.

Instrument	⟨MJD⟩	ΔMJD (day)	N	MAGZP (mag)	w2mcor (mag)	⟨w2mag⟩ (mag)	σ (mag)
WISE	55 263.89	0.99	13	19.596	0.331	10.155	0.037
WISE	55 455.11	1.12	15	19.692	0.331	10.226	0.037
NEOWISE-R	56 726.88	4.54	10	19.669	0.322	10.616	0.037
NEOWISE-R	56 918.17	4.87	16	19.642	0.322	10.888	0.038
NEOWISE-R	57 087.66	1.12	14	19.645	0.326	10.917	0.037
NEOWISE-R	57 281.94	1.25	16	19.641	0.326	11.137	0.038
NEOWISE-R	57 446.82	0.98	7	19.641	0.326	11.274	0.038
NEOWISE-R	57 649.88	8.78	17	19.644	0.326	11.599	0.038
NEOWISE-R	57 814.43	7.99	15	19.644	0.326	11.708	0.038
NEOWISE-R	58 013.16	1.11	16	19.643	0.326	12.557	0.042
NEOWISE-R	58 170.74	6.48	12	19.643	0.326	12.307	0.042
NEOWISE-R	58 377.31	1.11	13	19.643	0.326	12.565	0.045

Notes. The aperture photometry in each observing epoch was computed from coadded single exposures of a good quality. The aperture correction (w2mcor) is taken from the single exposure (L1b) source tables. The uncertainty of the magnitude zero-point (MAGZP) is fixed to 0.037 mag.

Wide-field Infrared Survey Explorer (NEOWISE) reactivation mission (Mainzer et al. 2014) in 2014–2019 for which several single exposures were obtained at each observing epoch[2].

The All-Sky, WISE 3-band Cryo, and NEOWISE Reactivation 2015–2019 data releases provide single exposure (L1b) source tables for 2010 and 2014–2018. The profile-fit photometry of HOPS 383 in the W2 band at 4.6 μm is available from 2010 March to 2017 February. As the FWHM in the W2 band is limited to 6″, HOPS 383 lies on the wing of the PSF of a brighter source (2MASS J05353060−0459360), which is located at 15.″3 northeast. This profile fit computed on $1.5 \times FWHM$ in radius mitigates this contamination. For each observing epoch, we selected the best profile-fit fluxes ($w2rchi2 \leq 2$) from the best single-exposure frames ($qual_frame > 0$, $qi_fact > 0$, $saa_sep > 0$, and $moon_masked = 0$) and we computed the mean and standard deviation of these fluxes. The mean profile-fit flux decays by 2.1 ± 0.2 mag in 7 years (black dots in Fig. B.1 and Table B.1).

For each observing epoch, we selected the W2-band frames of a good quality ($qual_frame > 0$) and stacked them with the WISE/NEOWISE coadder[2] using simple area weighting and a pixel scale of 1.″375 for the final image. HOPS 383 is still visible after 2017 February in these stacked images as a faint source. To obtain aperture photometry, we used a standard 8.″25 radius aperture centered on the *Spitzer* position of HOPS 383 (Megeath et al. 2012) and a custom 11″ radius background-aperture located 22″ west of it, on a region free of point sources with lower extended emission compared to the 50″−70″ radius annulus used in the single exposure source tables. The aperture correction (w2mcor) is taken from the single exposure (L1b) source table. The uncertainty of the magnitude zero-point (MAGZP) is fixed to the value of the WISE all-sky single exposures ($\sigma_{\rm MAGZP} = 0.037$ mag). The aperture flux decays by 2.40 ± 0.06 mag in 7.5 years (white dots in Fig. B.1 and Table B.2), which is consistent with the behavior of the profile-fit flux, despite contaminating sources in the source aperture. The aperture flux increases by 0.25 ± 0.06 mag between 2017 September and 2018 February, before coming back in 2018 September to the lower level that was observed previously. We conclude that the decay of the 2008 accretion outburst ended by 2017 September, which was three months before our *Chandra* observations (Table C.1).

Appendix C: *Chandra* ACIS-I data

C.1. Observations

The *Chandra* observations are listed in Table C.1.

Table C.1. Log of *Chandra* observations with ACIS-I (PI: N.G.).

ObsID	Start time (UT)	Exposure (s)
18927	2017-12-13T04:00:48	37 411
20882	2017-12-14T01:24:04	32 652
20883	2017-12-14T17:09:31	13 814

C.2. Data reduction

We used the CIAO package[3] (version 4.9 with the calibration database version 4.8.1; Fruscione et al. 2006) to reprocess the datasets (Table C.1) with the tool `chandra_repro`. The source detection was performed in each observation with the CIAO tool `wavdetect` with a detection threshold 1×10^{-5} and including information from the PSF. Twelve images were used per ObsID corresponding to three energy bands (0.5–2, 2–7, and 0.5–7 keV) and four resolution images (0.″25, 0.″5, 1″, and 2″) that were searched for with `wavdetect` on various pixel scales (1–2, 1–4, 1–8, and 1–16 pixel scales, corresponding to 0.″5–1.″5, 1″–8″, and 2″–32″, respectively) to mitigate the spatial variation of the PSF on the detector (Broos et al. 2010). The obtained `wavdetect` source lists were then merged by pairs using the source matching IDL program `match_xy` in the Tools for ACIS Review & Analysis (TARA) package[4] (Broos et al. 2010).

The events were extracted using the ACIS Extract (AE) software package[5] (version ae2018june14; Broos et al. 2010)

[2] https://irsa.ipac.caltech.edu/Missions/wise.html

[3] https://cxc.cfa.harvard.edu/ciao/

[4] http://personal.psu.edu/psb6/TARA/

[5] http://personal.psu.edu/psb6/TARA/ae_users_guide.html

following the multi-pass validation procedure (revision 1099 of 2018-06-11)[6]. The AE source apertures were centered on source positions with a default PSF fraction of 90% at 1.49 keV, which was determined from point source simulations computed by ray-tracing with MARX (Davis et al. 2012). The AE background regions were built to get enough background counts in order to have the source photometry errors within 3% of the values that would be obtained with no uncertainty in the background. New positions were determined for isolated sources with an off-axis position lower than 5′ using the mean position of the extracted events. These positions were used to determine the astrometric position offsets between the ObsIDs and a reference catalog. We used the *Gaia* data release 2 (DR2)[7] positions and position errors (Gaia Collaboration 2016, 2018) that we propagated with `topcat`[8] (Taylor 2019) from the J2015.5 reference epoch to the J2017.948 *Chandra* epoch (using the same zero radial velocity and radial velocity error as in the Celestia 2000, HIPPARCOS and *Tycho* catalog) and added 2MASS sources without the *Gaia* DR2 best neighbor (Marrese et al. 2019); we excluded a 2MASS source that was resolved by *Gaia* and *Chandra*. The new positions were also determined for isolated sources with an off-axis position larger than 5′ using the PSF correlation position. For crowded sources (PSF fraction <87%), the peak in a maximum-likelihood image reconstruction was used. The correlation and reconstruction were performed using a multi-ObsID event image and a composite PSF image. These steps were repeated until converging to no offsets between the ObsIDs.

C.3. Astrometry

The final X-ray positions are mainly registered on *Gaia* DR2 (with 45 *Gaia* and 12 2MASS sources), that is to say, on the ICRS world coordinate system. The position of the X-ray counterpart of HOPS 383 converted to the J2000 world coordinate system is $05^{\rm h}35^{\rm m}29\overset{\rm s}{.}789$, $-04^\circ59'50\overset{''}{.}432$ with a positional error of $0\overset{''}{.}099$ that includes, added in quadrature, the first-ObsID reference offset uncertainty of $0\overset{''}{.}029$ to the AE positional error of $0\overset{''}{.}095$ (Eqs. (1)–(3) in Broos et al. 2010).

The radio position of JVLA-SE and NW in Figs. 1b and c were determined from the pixel maximums in Fig. 1 of Galván-Madrid et al. (2015) converted to grayscale, assuming a J2000 world coordinate system, with positional errors estimated using $FWHM/(2\sqrt{2\ln 2}\,S/N)$, where S/N is the signal-to-noise ratio. For the *Spitzer* counterpart, we adopted a conservative position error of 1″, corresponding to the matching radius used in Megeath et al. (2012).

C.4. Timing analysis

The source aperture with a PSF fraction of 96% was used for the timing and spectral analysis of HOPS 383. The background is negligible (Appendix C.5). We estimated the count rates versus time ($\widehat{CR}$) from the arrival time (t_i) of the events ($N = 28$) with a kernel estimator of the density ($\widehat{f}$; Feigelson & Jogesh Babu 2012) with a constant bandwidth (h): $\widehat{CR}(t,h) = N\widehat{f}(t,h)/\mathrm{DTCOR}$, where DTCOR = 0.98693 is the deadtime correction and $\widehat{f}(t,h) = (1/hN) \times \sum_{i=1}^{N} K\{(t-t_i)/h\}$, where we used the Epanechnikov kernel, the inverted parabola defined as $K(y) = 0.75\,(1-y^2)$ with $-1 \le y \le 1$. We chose for h: the rule-of-thumb bandwidth, $h_{\rm rot}$, designed for unimodal distribution (Eq. (6.9) in Feigelson & Jogesh Babu 2012, and cyan curve in Fig. 2c); and the optimal bandwidth, $h_{\rm cv}$, maximizing the cross-validation (Eq. (6.10) in Feigelson & Jogesh Babu 2012, and green curve in Fig. 2). The latter is ∼3.6 larger than the former, producing a smoother light curve in particular at the end of the X-ray burst.

Then, we used an adaptive (bandwidth) kernel estimator (Eqs. (6.14)–(6.15) in Feigelson & Jogesh Babu 2012) with the recommend value of 0.5 for the sensitivity parameter α. This was computed from the pilot densities previously obtained with $h_{\rm rot}$ (blue curve in Fig. 2c) and $h_{\rm cv}$ (red curve in Fig. 2c).

C.5. Spectral analysis

The source-plus-background spectrum was limited to the flare time interval ranging from the first to the last detected event and the 0.5–9.9 keV energy range. An energy-dependent aperture correction was applied by AE to the ancillary response file, which calibrates the extraction. The background spectrum was extracted from the full exposure of the first observation in the 0.1–10 keV energy range.

The simultaneous spectral fitting of the background and source-plus-background spectra was made with XSPEC[9] (version 12.10.1) using the C-statistic applied to unbinned data. The background cumulative spectrum was modeled with the AE `cplinear` model, a continuous piecewise-linear function with ten vertices (Broos et al. 2010). The source spectrum was modeled with an interstellar medium absorption (Wilms et al. 2000) and an isothermal collisional-radiative plasma (Smith et al. 2001) with the typical coronal abundances of pre-main sequence stars (Güdel et al. 2007) plus an emission line with zero width at 6.4 keV (`TBabs*(vapec+gaussian)`) to which the background model, re-scaled to the source aperture, was added to fit the source-plus-background cumulative spectrum (data flow diagram in Fig. 10 of Broos et al. 2010). The model parameters, namely the hydrogen column density, the plasma temperature and normalization, the line normalization, and the ten parameters of `cplinear`, were first estimated by C-statistic minimization (C-stat = 677.0 using 1309 degrees of freedom; Fig. C.1a). The emission line was added to improve the modeling below ∼6.4 keV (C-stat = 671.8 using 1308 degrees of freedom; Fig. C.1b).

We fixed the `cplinear` parameters since the background contribution to the source-plus-background spectrum (0.1 count) was negligible. We performed a Markov chain Monte Carlo (MCMC; Hogg & Foreman-Mackey 2018) to compute the probability density functions of the four physical parameters of this model using the Jeremy Sanders' `xspec_emcee` program[10] that used a Python implementation of the MCMC ensemble sampler with affine invariance proposed by Goodman & Weare (2010), `emcee`[11] (version 2.2.1; Foreman-Mackey et al. 2013). We customized `xspec_emcee` to output subsidiary Markov chains for the acceptance fraction (Foreman-Mackey et al. 2013) and the following physical values: soft and hard fluxes; soft and hard absorption-corrected fluxes; and line equivalent width and counts. We used uniform priors for the physical parameters, $N_{\rm w} = 46$ walkers that were started clustered around the previous parameter estimates, and $N_{\rm iter} = 10^6$ iterations.

[6] http://personal.psu.edu/psb6/TARA/procedures/
[7] http://gea.esac.esa.int/archive/
[8] http://www.star.bris.ac.uk/~mbt/topcat/
[9] https://heasarc.gsfc.nasa.gov/xanadu/xspec/
[10] https://github.com/jeremysanders/xspec_emcee
[11] https://emcee.readthedocs.io/en/v2.2.1/

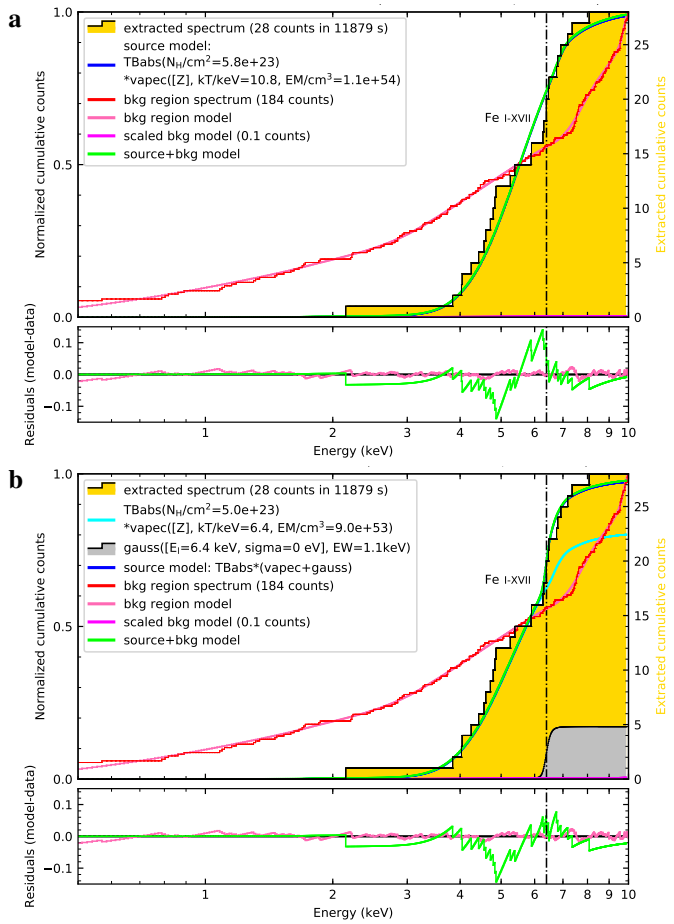

Fig. C.1. X-ray spectrum of HOPS 383 and background determination. *Panels a and b*: *top panels*: source-plus-background extracted cumulative spectrum (gold filled area) and XSPEC best-fit model (green), source model (blue), background region cumulative spectrum (orange) and model (red), and scaled background model (pink). The vertical dashed-dotted line is the energy of the 6.4 keV line arising from neutral or low-ionization iron. *Bottom panels*: model-minus-data residuals. *Panel b*: absorbed coronal thin emission (cyan) and 6.4 keV Gaussian emission line (silver filled area).

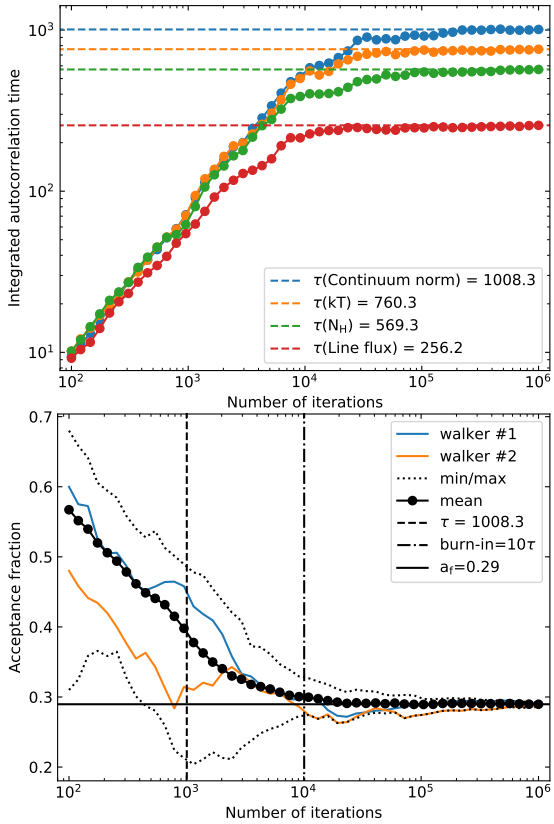

Fig. C.2. Burn-in phase of the MCMC samples. *Top panel*: estimator of the integrated autocorrelation time versus the number of iterations. The dashed horizontal lines are the integrated autocorrelation time in an iteration-number unit for the model parameters after 10^6 iterations with 46 walkers; the burn-in phase is lower than ten times the maximum of these values. *Bottom panel*: acceptance fraction versus the number of iterations. The mean of the walkers' acceptance fractions (dotted line) converges after the burn-in phase.

To test for convergence of the Markov chains, we followed Hogg & Foreman-Mackey (2018) by using the integrated autocorrelation time that we computed for each walker and then averaged these estimates[12] for each parameter, and retained the largest value, τ (top panel of Fig. C.2). The MCMC burn-in phase was supposed to last less than $N_{\text{burn-in}} = 10\tau = 10\,008$ iterations (Foreman-Mackey et al. 2013), as this was illustrated by the mean of the walkers' acceptance fractions converging to ~0.3, which is well within the recommended range (Foreman-Mackey et al. 2013) of 0.2–0.5 (bottom panel of Fig. C.2b).

This MCMC burn-in phase was cut-off before producing the corner plots (Fig. C.3a) from which the parameter median values and 90% confidence interval[13] were determined (Table C.2). For comparison purposes, Fig. C.4 shows the source-plus-background extracted cumulative counts spectrum (gold), the model for the parameter median values (green), and a random subset of 200 MCMC models (gray).

In this MCMC, the number of effectively independent data points is $N = (N_{\text{iter}} - N_{\text{burn-in}}) \times N_{\text{w}} \approx 4.6 \times 10^7$ and the relative accuracy is $100\sqrt{\tau/N} = 0.5\%$. The probability of the emission line was computed as the probability to have at least 0.5 count from this line (Fig. C.3b).

C.6. Quiescent luminosity

We used the CIAO tool `aprates` to compute the source count rate in the 2–8 keV energy band during our observations and excluding the flare time interval, which led to a live time of ~72 000 s. The source-plus-background aperture centered on the source position had an area of ~2.4″^{2} and corresponding to a PSF fraction of 90% at 1.49 keV. The background aperture was a ~2″.5 – ~30″ annulus centered on the source position where the neighbor source region was excluded with an area of ~2700″^{2}, corresponding to a PSF fraction of 0.9% at 1.49 keV. The total counts in source-plus-background and background apertures were 1 (at 3.0 keV) and 304, respectively. Inside the source-plus-background aperture, we estimated a quiescent source count rate of 0.011 count ks^{-1} (0–0.057 count ks^{-1}, 90% C.I.).

From a `tbabs*vapec` model with $N_{\text{H,X}} = 7.0 \times 10^{23}$ cm^{-2} and a typical plasma quiescent temperature ($kT = 1$ keV), we determined, using XSPEC, that the aperture corrected, observed

[12] See Dan Foreman-Mackey's blog on autocorrelation time estimation (2017 October 16): https://dfm.io/posts/autocorr/.

[13] We followed Hogg & Foreman-Mackey (2018), who are in favor of reporting median and quantiles, which are based on integrals, and against mode, which is not.

Table C.2. Markov chain Monte Carlo results on the flare time interval.

Parameter name	Symbol	Value		Unit
		Median	90% C.I.	
	Absorption			
Hydrogen column density	$N_{\rm H,X}$	7.0	3.9–10.5	10^{23} cm^{-2}
	Plasma emission			
Temperature	kT	4.1	1.3–17.8	keV
	T	47.1	15.2–207.0	MK
Emission measure [(a)]	EM	2.1	0.5–32.5	10^{54} cm^{-3}
Hard-band intrinsic luminosity [(a)]	$L_{\rm X,intr}$(2–8 keV)	1.7	0.7–7.2	10^{31} erg s^{-1}
Soft-band intrinsic luminosity [(a)]	$L_{\rm X,intr}$(0.5–2 keV)	1.2	0.3–22.7	10^{31} erg s^{-1}
Full-band intrinsic luminosity [(a)]	$L_{\rm X,intr}$(0.5–8 keV)	3.0	0.9–29.9	10^{31} erg s^{-1}
	Neutral to low-ionization iron line emission			
Line flux	Flux(Fe 6.4 keV)	6.1	1.7–14.1	10^{-6} ph cm^{-2} s^{-1}
Equivalent width	EW(Fe 6.4 keV)	1.1	0.2–3.1	keV
Total count number	N(Fe 6.4 keV)	5.1	1.4–10.8	counts

Notes. [(a)]Assuming a distance of 420 pc (Safron et al. 2015).

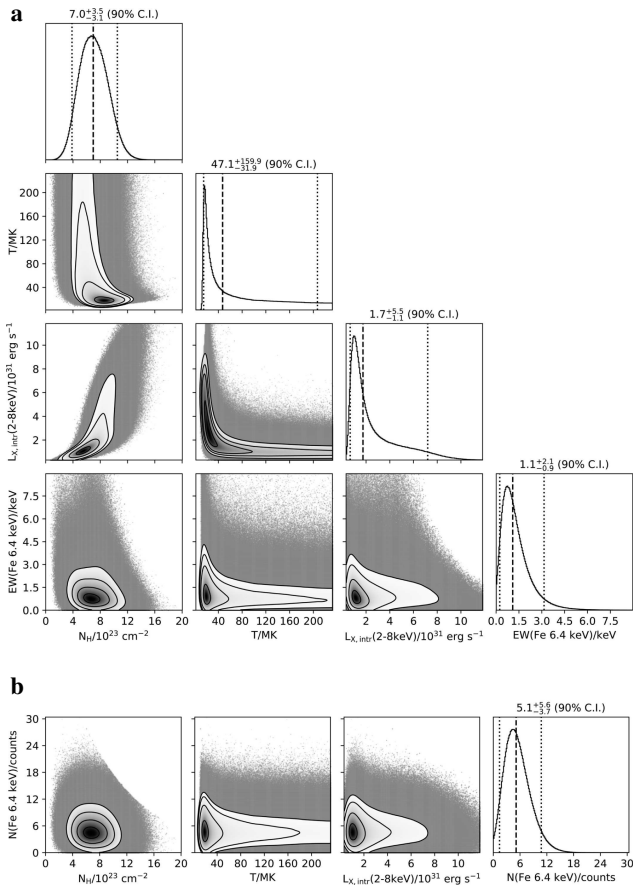

Fig. C.3. Posterior probability and covariance distributions of the flare-emission model parameters. *Panel a*: hydrogen column density, plasma temperature, X-ray intrinsic luminosity in the 2–8 keV range, and equivalent width of the Fe line at 6.4 keV. The size of the MCMC samples is about 4.6×10^7 with about 4.5×10^4 independent MCMC samples. The dashed and dotted vertical lines in the diagonal plots show the median value and the 90% confidence interval (C.I.) for each parameter. The contours in the other plots are 11.8, 39.3, 67.5, and 86.5% C.I. (corresponding to 0.5, 1, 1.5, and 2σ levels for a 2D Gaussian) for each pair of parameters. *Panel b*: alternative last row with count number from the emission line.

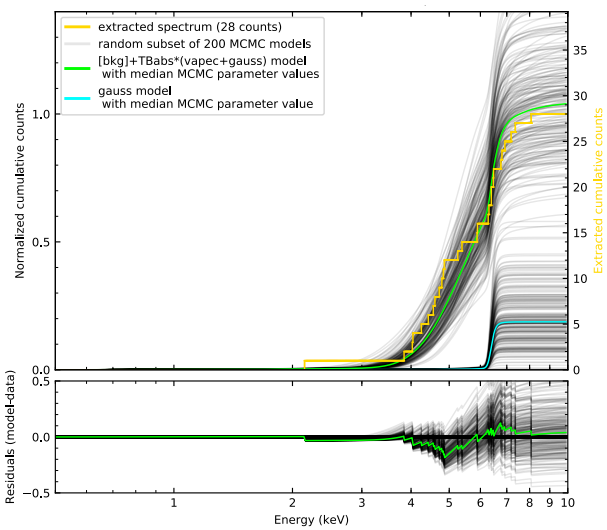

Fig. C.4. X-ray spectrum of HOPS 383 and Markov chain Monte Carlo (MCMC) models. *Top panel*: source-plus-background extracted cumulative spectrum (gold) and median MCMC model (green), 6.4 keV Gaussian emission line with median MCMC model (cyan), and a random subset of 200 MCMC models (gray). *Bottom panel*: model-minus-data residuals.

flux and absorption-corrected luminosity were lower than 2.0×10^{-15} erg cm^{-2} s^{-1} and 2.0×10^{30} erg s^{-1} in the 2–8 keV energy band, respectively.

Appendix D: SOAR Spartan data

D.1. Observations

The Spartan observations are listed in Table D.1.

D.2. Data reduction

An end-to-end pipeline, THELI[14] (version 1.9.5; Schirmer 2013), was used for the reduction of the calibration and

[14] https://www.astro.uni-bonn.de/theli/

Table D.1. Log of SOAR observations with Spartan (proposal ID 2016B-0930, PI: N.G.; observers: K.H. and D.P.).

Filter	Wavelength (microns)	Width (microns)	Start time (UT)	DIT [(a)] (s)	NDIT [(b)]	Exposure [(c)] (s)	*FWHM* [(d)] (arcsec)
K	2.148	0.307	2017-12-14T01:01:22	179.98	37	6659.26	1.0
H_2	2.116	0.031	2017-12-14T03:47:50	240.09	11	2640.99	1.0

Notes. We also obtained standard infrared calibration data: dark exposures and dome flat exposures with the lamp on and off to account for the thermal emission from the telescope. [(a)]Detector integration time. [(b)]Number of frame exposures with the target. [(c)]Total exposure of the stacked dithered frames. [(d)]Image quality of the stacked dithered frames.

observation data (Table D.1) obtained with det3, including astrometry with `SExtractor` (Bertin & Arnouts 1996) and `SWarp` (Bertin et al. 2002). We wrote a custom IDL program to automatically detect and correct, in the dark and flat-field corrected frames, any residual bulk images that were produced by bright stars, close to saturation in the raw frames. In each raw frame, this program identified any saturated regions centered on bright stars and looked at these detector positions in the subsequent calibrated frames for any excess above the sky level by fitting a constant level or a parabola (based on an F-test). These excesses were then subtracted or masked when too close to a source. These calibrated and corrected images were registered using the 2MASS catalog and stacked using median values and a pixel scale of 0″.5.

In the H_2 narrow-band filter image, the shocked molecular hydrogen emission has a higher S/N compared to the *K*-band image. We produce for validation a pure H_2 emission image by subtracting the *K*-band image scaled by a factor that we obtain by minimizing the residuals on stars in the final image (Navarete et al. 2015).

Appendix E: Density model

We started from the protostellar model of HOPS 383, which is composed of an accretion disk in an infalling envelope with bipolar cavities (Furlan et al. 2016). The fixed parameters in this model grid (Table 3 of Furlan et al. 2016) that was computed with the Monte Carlo radiative transfer code, `ttsre`[15] (2008 version; Whitney et al. 2003) were:

– the stellar mass ($M_\star = 0.5\,M_\odot$),

– the stellar effective temperature ($T_\star = 4000$ K),

– the disk mass ($M_{\rm disk} = 0.05\,M_\odot$),

– the magnetospheric truncation radius of the gas disk ($R_{\rm trunc} = 3\,R_\star$),

– the dust-disk inner radius (set to the dust sublimation radius, $R_{\rm sub}/R_\star = (T_{\rm sub}/T_\star)^{-2.1} = 6.8$ where $T_{\rm sub} = 1600$ K is the dust sublimation temperature; Whitney et al. 2003),

– the scale height of the disk at the dust sublimation radius (set to the hydrostatic equilibrium solution; Eq. (35) of D'Alessio et al. 1998),

– the mean molecular mass per hydrogen nucleus ($\mu = 2.3$),

– the radial ($A = 2.25$) and vertical ($B = 1.25$) exponent in disk density law,

– the fractional area of the hot spots on the star ($f_{\rm spot} = 0.01$),

– the envelope outer radius ($R_{\rm env} = 10\,000$ au),

– the centrifugal radius of the envelope ($R_{\rm c} = R_{\rm disk}$),

– the exponent of the cavity polynomial shape ($b_{\rm cav} = 1.5$), and

– the vertical offset of the cavity wall ($z_{\rm cav} = 0$ au).

The best-fit parameters for HOPS 383 (Table 1 of Furlan et al. 2016) were:

– the stellar radius ($R_\star = 6.61\,R_\odot$),

– the disk outer radius ($R_{\rm disk} = 5$ au; we note that the opacity was dominated by the envelope in these SED models, which did not directly constrain the size of the disk; Furlan et al. 2016),

– the envelope (gas and dust) density at 1000 au ($\rho_{1000} = 1.78 \times 10^{-17}$ g cm^{-3}) and, as $\rho_{1000} \propto \dot{M}_{\rm env}$, the envelope infall rate ($\dot{M}_{\rm env} = 7.48 \times 10^{-5}\,M_\odot$ yr^{-1}),

– the cavity opening angle ($\theta = 45°$),

– the stellar luminosity ($L_\star = 10\,L_\odot$),

– the total (star and accretion) luminosity ($L_{\rm tot} = s \times 30.2\,L_\odot = 55.49\,L_\odot$, where $s = 1.84$ is the luminosity scaling factor to match the observed SED flux, Eq. (3) of Furlan et al. 2016),

– the inclination angle ($i = 69.5°$; corresponding in the model grid to $\cos i = 0.35$ with a sampling step of 0.1), and

– the foreground cloud extinction ($A_{\rm V,cloud} = 14$ mag; corresponding to $N_{\rm H,cloud} = 14 \times 10^{21}$ cm^{-2}, as $N_{\rm H,cloud}/A_{\rm V,cloud} = 1.0 \times 10^{21}$ cm^{-2} mag^{-1} in Furlan et al. 2016).

To be consistent with the luminosity scaling factor (s), we introduced s', a scaling factor for the disk-to-star accretion rate ($\dot{M}_{\rm disk}$). Indeed, the above values of $R_\star$ ($6.61\,R_\odot$), $L_\star$ ($10\,L_\odot$), and $L_{\rm tot} = L_\star + L_{\rm acc}$ ($30.2\,L_\odot$) correspond in the model grid to $\dot{M}_{\rm disk} = 1.14 \times 10^{-5}\,M_\odot$ yr^{-1}, since $L_{\rm acc} \propto \dot{M}_{\rm disk}$, we set $s' = 2.25$ and hence $\dot{M}_{\rm disk} = 2.57 \times 10^{-5}\,M_\odot$ yr^{-1}.

The envelope density was given by Eqs. (1) and (2) of Whitney et al. (2003). We note that the bipolar cavities in Furlan et al. (2016) are free of dust (and gas); for consistency, we filled them in with gas, using a constant density ($n_{\rm H_2} = 2 \times 10^4$ cm^{-3}; Whitney et al. 2003).

The disk density was given by Eq. (3) of Whitney et al. (2003) and normalized to $M_{\rm disk}$ from $R_{\rm trunc}$ to $R_{\rm disk}$ using a spherical outer boundary (Fig. 3b this work and Fig. 2b of Whitney et al. 2003). We added accretion funnels at $R_{\rm trunc}$, which were dust-free as located inside the dust sublimation radius, assuming for simplicity a dipole geometry for the magnetic field (Hartmann et al. 1994), and using $f_{\rm spot}$ to compute a latitude band between the smallest and largest magnetic loops at the stellar surface. The accretion-funnel density was given by Eq. (9) of Hartmann et al. (1994).

The values of $N_{\rm H}$ along the line-of-sight were computed by numerically integrating these density equations. In this model grid, the gas-to-dust ratio is $R = 100$ and the protostellar dust opacity in the visible is $\kappa_{\rm ext,V} = 5.3 \times 10^4$ cm^2 g^{-1} (Fig. 6 of Ormel et al. 2011, (ic-sil,gra) at 0.3 Myr), leading to: $N_{\rm H}/A_{\rm V} = \ln 10 \times (1 + R)/(2.5\,\mu\,m_{\rm H}\,\kappa_{\rm ext,V}) = 4.6 \times 10^{20}$ cm^{-2} mag^{-1} where $m_{\rm H}$ is the hydrogen mass. Therefore, the observed $N_{\rm H,X}$ corresponds to $A_{\rm V} \sim 1500$ mag.

[15] https://gemelli.colorado.edu/~bwhitney/codes/codes.html